ALE Model: Air Cushion Impact Characteristics of Seaplane Landing Application

Yunsong Zhang, Ruiyou Li Shi*, Bo Gao, Changxun Song, Zhengzhou Zhang

State Grid Electric Power Space Technology Company Limited, Beijing, 102213, China

Abstract—Seaplane landing is a strong nonlinear gas-liquid-solid multiphase coupling problem, and the coupling impact characteristics of air cushion are very complicated, and it is difficult to maintain the stability of the air-frame. In this paper, The ALE method is used to study the landing of seaplane at different initial attitude angles and velocities. Firstly, a comparative study of the structure entry model and the air cushion effect model of flat impact water surface is conducted to verify the reliability of the numerical model in this paper, and the influence of the velocity, the water shape and the air cushion are accurately analyzed. Then, a seaplane landing is systematically studied, and the vertical acceleration, attitude angle, aircraft impact force and flow field distribution are analyzed. The results show that the air cushion has a great influence on the landing of seaplane. The smaller the initial horizontal velocity, the more obvious the cushioning effect of the air cushion. Cavitation causes a secondary impact on the tail and produces a pressure value exceeding the initial value, which may cause damage to the aircraft structure. The air cushion has a buffering effect on the seaplane, the pitch angle increases at a slower rate and the pressure value at the monitoring point decreases. The larger the initial attitude angle, the more significant the air cushion. By analyzing the landing rules of seaplane, the range of speed and attitude angle suitable for seaplane takeoff and landing process is given. The results of this paper can provide theoretical guidance for the stability design of seaplane takeoff and landing process.

Keywords—*Seaplane; ALE method; multiphase coupling; air cushion*

I. INTRODUCTION

Seaplanes can take off and land on water surface such as rivers, lakes, and seas. They possess notable characteristics, including excellent maneuverability, accessibility, high safety, and scalability. Seaplanes can operate on both water and land, reducing their dependence on specific geographical environments and the need for dedicated airport runways [1, 2]. However, the takeoff and landing process of seaplanes presents a challenging problem characterized by strong nonlinear gas-liquid-solid multiphase coupling. This process needs to consider anti-sinking ability, static stability, surface maneuverability, etc. Moreover, the presence of strong impacts further complicates this problem [3, 4].

Recent research on seaplanes has primarily focused on fluid-structure coupling algorithms, air cushion effects, and structural impact mechanisms. Regarding fluid-structure coupling algorithms, Iwanowski et al. [5] conducted numerical investigations on the horizontal rigid body impacting a water surface and analyzed the influence of compressible air cushions. The governing equations for air and water (modeled as compressible and non-compressible fluids, respectively) are solved using finite difference and fluid volume (VOF) methods. Mori Y et al. [6] combined the discrete element method (DEM) with computational fluid dynamics (CFD) to theoretically derive the stability condition of the drag term and develop a new implicit algorithm. The compatibility of the implicit algorithm with the boundary model composed of symbolic distance function and immersed boundary method is verified by experiments. Hessenthaler et al. [7] integrated several independent analytical solutions into a comprehensive framework, demonstrating its utility in analyzing convergent behavior and introducing novel fluid-structure interaction (FSI) algorithms. Han K et al. [8] validated the applicability of the coupled Boltzmann method (LBM) and discrete element method (DEM) in solving irregular particle transport in turbulence, employing test cases involving polygonal and super-quadratic particle transport in high Reynolds number fluid flows. Oger et al. [9] applied smooth particle hydrodynamics (SPH) method to simulate the solid-liquid coupling problem in a free-surface flow environment, and proposed a new formula of spatial variation resolution with variable smoothing length. Panciroli R et al. [10] investigated the fluid elasticity of an elastic wedge using a coupled finite element method and smooth particle hydrodynamics (FEM-SPH) method. The numerical simulation results agreed well with experimental data, accurately predicting the influence of hydro-elasticity on water impact involving the elastic wedge. Ahmadzadeh M et al. [11] employed the coupled Euler-Lagrange (CEL) method to study the impact of a sphere in free fall motion. Facci et al. [12] utilized the volume of fluid (VOF) method, based on the finite volume method, to simulate free surface multi-phase flows. They numerically analyzed the water impact phenomenon on a moving body and obtained the multi-phase flow field and surface pressure distribution on the body. Servan-Camas et al. [13] applied the SPH-FEM coupling model to analyze the liquid sloshing problem in the navigation body. Aquelet N et al. [14] proposed the Euler-Lagrange coupling algorithm, using a penalty function to calculate the coupling force at the fluid-structure interface and predict the local pressure peak on the structure. Fourey et al. [15] compared two fluid-structure coupling algorithms, parallel interleaving and sequential interleaving [16]. They found that the latter exhibited higher accuracy and stability but lower computational efficiency.

During the takeoff and landing process, the fuselage structure of a seaplane experiences significant friction or collision with the water body, while the presence of an air cushion adds complexity to the dynamics of the structure. Chuang [17] found that objects with small dead corners are more likely to form an air cushion when entering water. The air

---

*Corresponding Author.

cushion between the model and the water surface plays an important role in the impact process. Song et al. [18] compared different shapes of air cushion, analyzed the structure of air cushion with different volume, and analyzed the influence of different volume of air cushion on the peak value of water entry impact force of buoy. Ermanyuk and Ohkusu [19] designed a flat-bottom disk slamming experiment to study the influence of air cushion on the impact pressure. The presence of air cushion on the surface strongly affects the impact time scale and the shape of the splash jet. Chen Zhen et al. [20] used MSC. Dytran to simulate the mixing of air layer and water surface, and made a detailed analysis on the formation of air cushion. They used the ALE method to observe the presence of a hollow air cushion during the water entry process of flat-bottomed structures, noting that the air cushion can be identified within the air cushion when the peak impact pressure occurs. They also employed a neural network method to fit the impact pressure results and predict the bottom impact pressure. Huera-Huare et al. [21] investigated the effects of different angles on models and their corresponding air cushion effects. They observed that when the water entry angle decreased to less than 5°, an air cushion formed with a significantly lower peak impact pressure than the theoretical value. When the exit angle exceeded 5°, the peak impact pressure followed von Kan's theory. Zhang Jian et al.[22] used numerical simulation to study the influence mechanism of hollow air cushion during the water entry of two-dimensional wedge. Fang et al. [23] studied the air cushion effect and impact load in two-dimensional flat plate water entry problem using the multi-phase Riemann-SPH method based on the PVRS Riemann-solver.

The structural impact problem involves the complex coupling of rigid bodies or deformable bodies with the movement of the surrounding flow field. This complexity is further heightened by the dynamic changes in the free surface and the interaction with air. Adam et al. [24] proposed a new surface tension formula that can deal with multi-phase problems with high density and viscosity ratios. Wang et al. [25] (2022) developed a strategy to eliminate gas phase tensile instability, ensuring computational stability. They also established Riemann models for different materials and obtained a robust gas-solid-liquid contact algorithm. Washino K et al. [26] (2020) proposed an interface capture method based on color function to improve the smoothness of the interface. Shi et al. [27] investigated the effects of head shape parameters, shell thickness, water entry velocity, and angle on the acceleration, pressure, stress, and structural deformation of an elastic underwater vehicle during water entry impact. Based on the fluid volume multi-phase flow model and dynamic grid technology, Liu et al. [28] established a coupling calculation method for the multi-phase flow field and trajectory of a cross-medium vehicle entering water at high speed.

Grid-free method is also often used to simulate the impact of structures [29]. Shao et al. [30] simulated the high-speed impact jet problem, and analyzed the pressure response rule on the wall. Shao et al. [31] established an improved Smoothed Particle Hydrodynamics (SPH) model, and analyzed the influencing factors and flow field changes during the water entry of slender objects. Yang et al. [32] proposed an SPH-EBG algorithm to simulate the impact of dam break flow on elastic plates. Khayyer

et al. [33] introduced a full Lagrange particle method under the Material Point Simulation (MPS) framework to simulate the influence of structural elastic response on water entry [34]. Sun et al. [35] improved the SPH method and conducted a simulation study on cylinder water entry problems [36]. Chen et al. [37] utilized MPS method to simulate the water entry problem of a two-dimensional wedge. They investigated the effects of different particle arrangements on calculated results, including vertical hydrodynamic force and free surface changes.

The take-off and landing of seaplane is a strong nonlinear gas-liquid-solid multiphase coupling problem, and it is necessary to consider the air cushion effect and impact effect during the movement. Theoretical analysis can establish clear relationships between changes in physical quantities and flow parameters, offering broad applicability. However, solving the nonlinear problem of air cushion impact is challenging. Experimental analysis often encounters scale effects between experiment models and actual motion due to the intricate topological shapes and external environment. Additionally, model testing requires a lengthy period, and in many cases, the experimental data is incomplete with inadequate repeatability. The grid method can get relatively accurate results when simulating small deformations, however, the VOF method or the level set method needs to be used to track the interface. The particle-type method has made significant progress in simulating severe fluid-structure coupling problems. However, there is a scarcity of full-fluid-structure coupling algorithms that consider the boundary layer effect on the structure's surface. In this paper, ALE method is used to study the landing of a seaplane. The coupled impact dynamic characteristics at different angles and entry speeds are analyzed, and the changes of air cushion are analyzed. The results of this paper have a good guiding significance for the development of seaplane.

II. METHODOLOGY

A. Fundamental Equations

In this paper, the ALE algorithm is used to describe the fluid domain. And the fluid-structure coupling algorithm based on penalty function and Lagrange method are used to simulate the landing process. The Euler coordinate system serves as a fixed fluid coordinate system, unaffected by the object's movement or deformation. The Lagrangian coordinate system acts as a fixed solid coordinate system, with its grid nodes attached to the material nodes. As the solid undergoes deformation, the solid coordinate system adjusts accordingly. The ALE coordinate system is independent of the Eulerian coordinate system and the Lagrangian coordinate system and is not completely fixed on space or solid nodes.

The ALE description introduces a reference domain independent of the material domain and the spatial domain, which always coincides with the grid throughout the calculation process. Fig. 1 shows the mapping relationship between the structural domain and the fluid domain. The mapping expression from the material domain to the spatial domain is as follows:

$$x = x(X, t) \tag{1}$$

The mapping from ALE reference domain to the spatial domain is:

$$x = w(w,t) \tag{2}$$

Since the reference domain always coincides with the grid, the transformation is performed:

$$w = w-1(x,t) \tag{3}$$

The mapping relationship of the material domain and the reference domain:
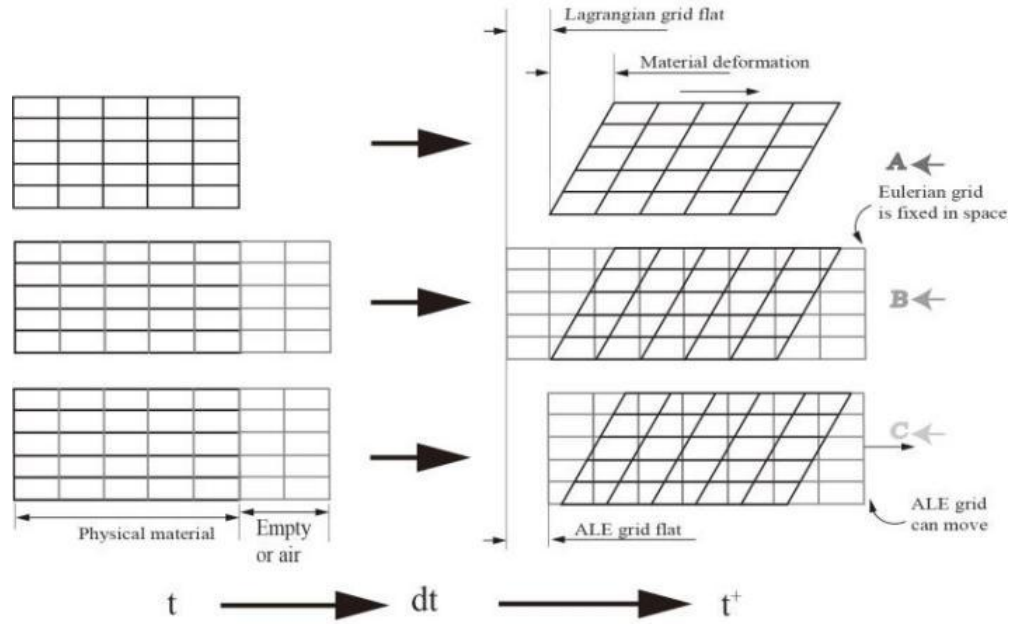
$$w = w-1[x(X,t),t] = v(X,t) \tag{4}$$

Fig. 1. Mapping between lagrange, euler, and ALE domains.

The expression of the mass equation is:

$$\frac{\partial \rho(\chi,\ t)}{\partial t} = -\rho \frac{\partial u_i}{\partial x_i} - c_i \frac{\partial \rho}{\partial x_i} \tag{5}$$

Where χ is the Lagrange coordinate system, x is the Euler coordinate system, ρ is the fluid density, and c_i is the relative velocity between the structure particle and the grid point in the reference coordinate system.

The equation of motion is:

$$\frac{\partial u_i(\chi,\ t)}{\partial t} = \frac{\partial \sigma_{ij}}{\partial x_j} + \rho b_i - c_j \frac{\partial u_i}{\partial x_j} \tag{6}$$

Where b_i is a unit force, in the Newtonian fluid, the stress tensor is related to the speed, the relationship is related:

$$\sigma_{ij} = \delta_{ij} P + \mu(\frac{\partial u_i}{\partial x_j} + \frac{\partial u_j}{\partial x_i}) \tag{7}$$

Wherein μ is a power viscosity coefficient, P represents pressure.

B. Contact Algorithm

In the contact algorithm, the contact force is proportional to the permeation vector in the time step. In the explicit finite element method, the contact algorithm calculates the interface force due to the influence of the structure on the fluid. These forces act on the fluid and structural nodes to prevent them from crossing the contact interface. The fluid utilizes either an ALE mesh or a Lagrangian grid [38]. In the contact algorithm, as shown in Fig. 2, one surface is designated as the contacting surface, while the second surface is the primary surface. The nodes located on these surfaces are respectively called slave nodes and primary nodes. For fluid-structural coupling problems, the fluid nodes on the interface are considered slave nodes, whereas the structural elements are treated as primary nodes. In this paper, a penalty-based contact method is employed. The force is applied from the slave node, and the force transmitted to the primary element node is scaled using a shape function. The corresponding expression is as follows:

$$F_s = -k_i \cdot d \tag{8}$$

$$F_m^i = N_i \cdot k \cdot d \tag{9}$$

The N_i is the shape function of the surrounding node i, (in 2D problems, the values are 1, 2; in 3D problems, the values are 1...4.). The coefficient k represents the stiffness of the spring, and d is a penetrating vector. If the node is completely

coincident from one of the primary nodes (see Fig. 2), the coefficient $k = 1$. Applying the Euler-Lagrangian coupling method to calculate the coupling force on the nodes can effectively prevent the large deformation of the grid.

$$F_s = -k_i \cdot d \qquad (10)$$

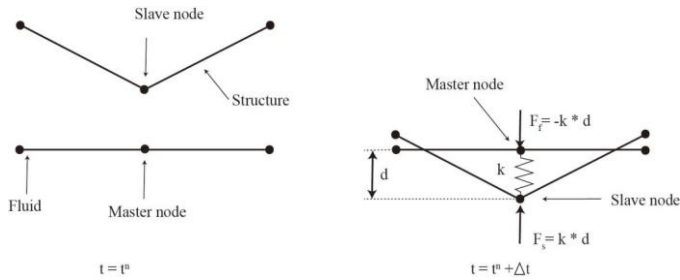$$F_m^1 = k \cdot d \ \ \alpha\nu\delta \ \ F_m^2 = F_m^3 = F_m^4 = 0 \qquad (11)$$

Fig. 2.   Schematic diagram of the contact algorithm.

III. NUMERICAL VERIFICATION

A. Water Entry

In order to verify the accuracy of the numerical model, this article first simulates the problem of a cylinder entering water. The aluminum solid cylindrical model has a length of 197 mm and a diameter of 50 mm, with a weight of 1.06 kg. It is subjected to an in-water angle of 60° and a speed of 4.35 m/s. Fig. 3 and Fig. 4 present the change in speed and acceleration of the cylinder, and Fig. 5 shows the simulation and experimental water entry process. It is observed that the numerical results before 0.12 s exhibit a strong agreement with the experimental results by Hou [39]. However, after 0.12 s, as the cavity begins to close, the pulsating pressure starts affecting the structure, leading to a decline in speed. Additionally, the simulated acceleration is slightly lower than the experiment.
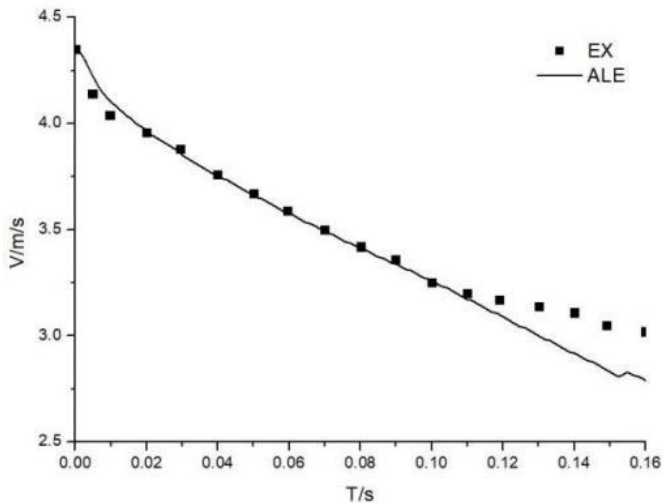
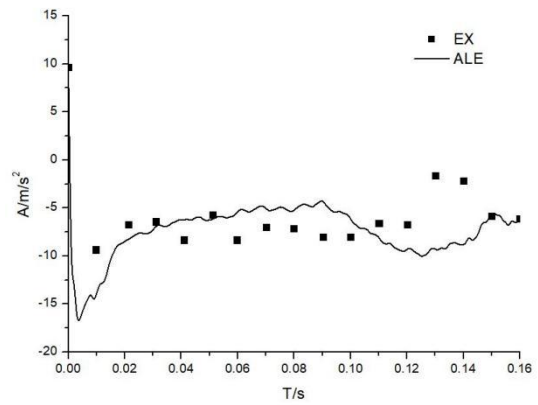Fig. 3.   Speed comparison between simulation and experiment [39]

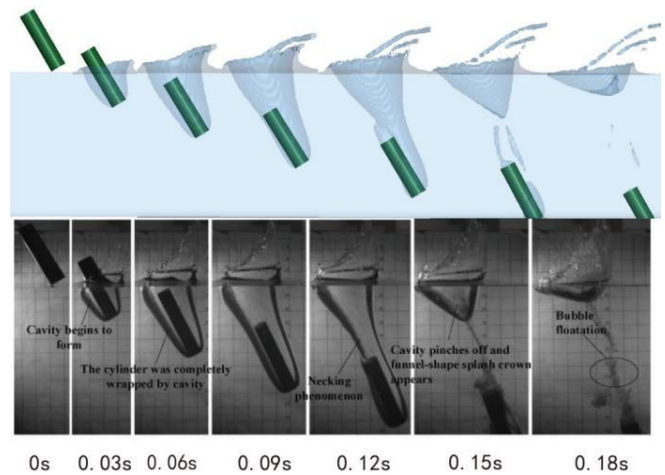Fig. 4.   Acceleration comparison between simulation and experiment [39].

Fig. 5.   The water entry of simulation and experiment [39].

B. Verification of Air Cushions

To validate the accuracy of the numerical model for the cushion effect, the same flat plate model as Ma et al. [40] was utilized. The impact plate employed has a mass of 32 kg, a length of 0.25 m, a width of 0.25 m, and a thickness of 0.012 m. By adjusting the initial position of the plate, an impact speed of 5.5 m/s was achieved.

Fig. 6 depicts the pressure curve at the center of the flat plate, and the simulation results exhibit favorable agreement with the experimental findings. The peak pressure slightly surpasses the experimental value, potentially attributed to the utilization of a bubble-generating device during the experiment, causing numerical fluctuations in the results. The pressure at the plate center only occurs momentarily within the structure, then air cushion is formed between the plate and the water surface, resulting in a pressure value of zero. Fig. 7 illustrates the impact force curve in the vertical direction, and the incorporation of the low-speed structure in this study does not exhibit a prominent air cushion effect. Additionally, Fig. 8 demonstrates the formation of an air cushion on the flat impact surface. As the plate continues to impact, the air cushion gradually increases, exerting minimal influence on the plate's impact.
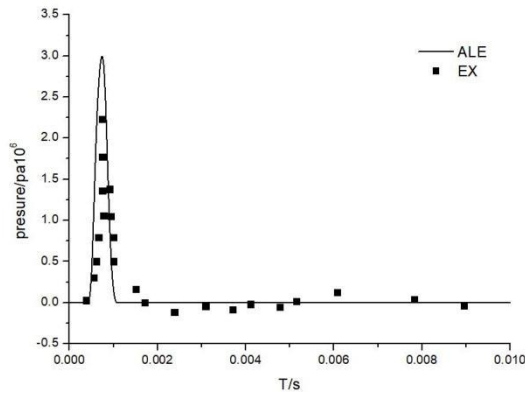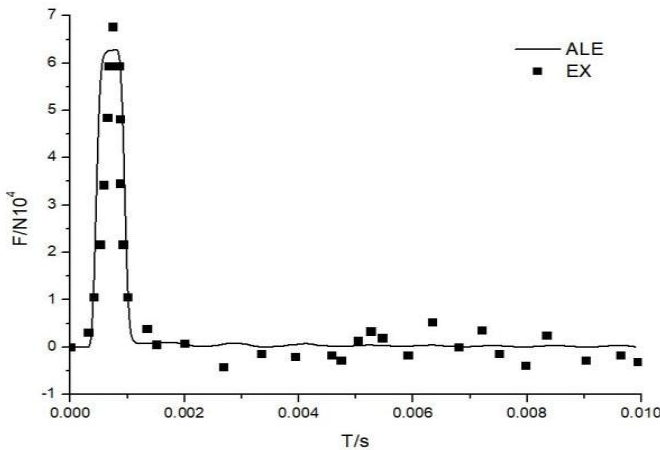
Fig. 6.   Pressure distribution on plate center.

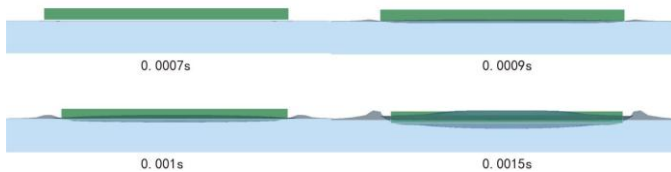Fig. 7.   Vertical impact force distribution of flat plate.

Fig. 8.   Air cushion effect during impact.

IV. NUMERICAL MODELS

A. Finite Element Model

Fig. 9 is a finite element model of a seaplane, which is simplified on the basis of the actual model. The aerodynamic effect is ignored, and it is assumed that the seaplane is completely rigid. The weight of the aircraft is 53500kg, the overall length is 37m, and the wing length is 38.4m. The size of water is 200m×50m×20m, the size of air is 200m×50m×200m. The centroid is situated at 30% of the average aerodynamic cord length, precisely aligned with the center of the wing roots. About two million meshes were used. In Fig. 9, the monitoring point P1 is positioned at the center of the aircraft fuselage, located 14.5 m from the aircraft's head. The boundary point P2 is situated 20 m from the seaplane's head, while P3 corresponds to the center position of the seaplane's bottom. The vertical distance between P2 and P3 is 0.6 m, with a horizontal separation of 14.2 m.
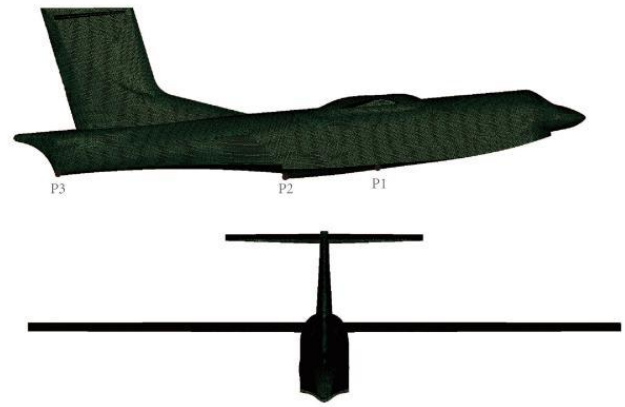

Fig. 9.   Aircraft model and grid.

B. Material Parameters

The Mie–Gruneisen equation of state is as follows:

$$P = \frac{\rho_0 C^2 \mu [1 + (1 - \frac{\gamma_0}{2})\mu - \frac{\alpha}{2}\mu^2]}{[1 - (S_1 - 1) - S_2 \frac{\mu^2}{\mu+1} - S_3 \frac{\mu^3}{(\mu+1)^2}]} + (\gamma_0 + \alpha\mu)E \quad (12)$$

Where E is in unit volume, C is the intercept of the $u_s - u_p$ curve, S_1, S_2 and S_3 are the unit-less coefficients of the slope of the $u_s - u_p$ curve. γ_0 is a Gruneisen parameter, α is a first-order correction value of γ_0. The compression ratio is related to the volume, defined as:

$$\mu = \frac{1}{V} - 1 \quad (13)$$

An equation can also be approximately:

$$P = \rho_0 C^2 \mu + (\gamma_0 + \alpha\mu)E \quad (14)$$

The polynomial state equation is selected for the air domain, and the internal energy of the initial volume changes linearly.

$$P = C_0 + C_1\mu + C_2\mu^2 + C_3\mu^3 + (C_4 + C_5\mu + C_6\mu^2)E \quad (15)$$

where, C1, C2, C3, C4, C5, C6 are the confident constant respectively.

The thickness of the rigid shell is 0.05m, and the density is 1257kg/m³. Table I shows the material parameters of the water and air domains.

TABLE I.   MATERIAL PARAMETERS

parameter	Density(kg/m³)	C	S₁	S₂	S₃	γ_0	V₀	E₀
water	1000	1480	1.92	-0.096	0	0.35	0	0
parameter	density(kg/m³)	C1	C2	C3	C4	C5	C6	E0
air	1.22	0	0	0	0.4	0.4	0	0

C. Landing setting

When the seaplane lands, it should maintain a certain speed and attitude angle. Fig. 10 is a schematic diagram of the initial water entry of the seaplane. Table II shows the settings of speed and attitude angle under different landing conditions.

TABLE II. SEAPLANE LANDING CONDITIONS

Serial number	1	2	3	4	5	6
horizontal velocity (m/s)	35	45	63.9	45	45	45
Vertical velocity (m/s)	1.5	1.5	1.5	1.5	1.5	1.5
angle(°)	5	5	5	5	8	10
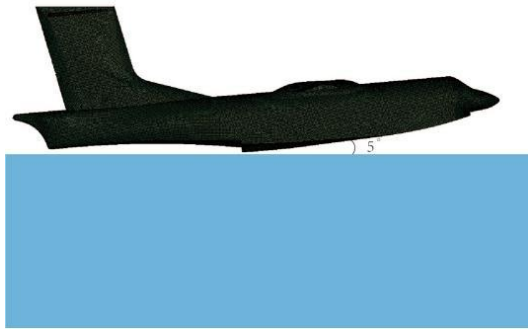
Fig. 10. Diagram of aircraft initial entry conditions.

V. RESULT AND ANALYSIS

A. Velocity Analysis

This paper systematically investigates the aircraft landing process, with an initial vertical velocity of 1.5 m/s. The variations in attitude angles and accelerations are analyzed for different initial horizontal velocities. The changes in the air cushion during the landing process are studied, along with the analysis of variations in impact force and pressure values at the monitoring point.

Fig. 11 illustrates the changes in vertical acceleration for an initial attitude angle of 5°. With an initial horizontal velocity of 35 m/s, the maximum vertical acceleration observed during the landing process is 12.17 m/s². For an initial horizontal velocity of 45 m/s, the maximum vertical acceleration reaches 13.14 m/s². When the initial horizontal velocity is further increased to 63.9 m/s, the maximum vertical acceleration during aircraft landing is 13.42 m/s². Notably, it is observed that the timing and magnitude of extreme acceleration remain similar across different horizontal velocities. Subsequent to the initial impact, the vertical acceleration exhibits relatively small fluctuations under higher horizontal velocity.

Fig. 12 shows the attitude angle change of the seaplane during landing when the initial attitude angle is 5°. For different initial speeds, the attitude angle of the seaplane initially decreases, then increases, and eventually decreases again. During the water impact process, the seaplane exhibits a forward inclination followed by a subsequent upward attitude. With an initial horizontal velocity of 35 m/s, the maximum attitude angle observed is 7.6°. When the initial horizontal velocity is 45 m/s, the maximum attitude angle reaches 7.64°. Finally, for an initial horizontal velocity of 63.9 m/s, the maximum attitude angle during water landing is 7.5°. By comparing the three curves in Fig. 12, it can be observed that for the same initial attitude angle,

the seaplane requires a longer time to tilt forward at higher speeds. Therefore, during the landing process, it is essential to choose an appropriate speed. Different speeds lead to varying pitch angles, influencing the position and timing of the seaplane's contact with the water surface, as well as its vertical acceleration.
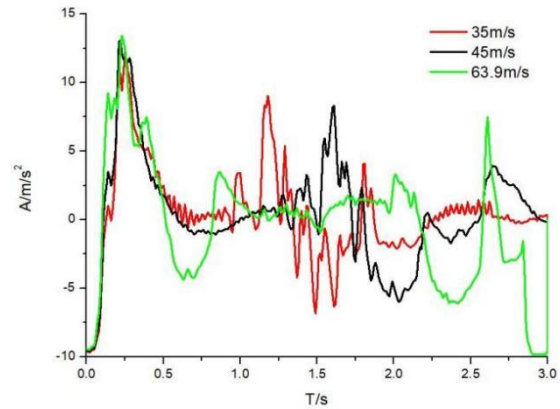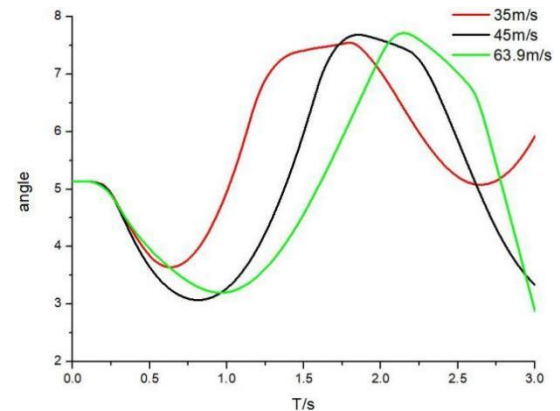

Fig. 11. Vertical acceleration curve.

Fig. 12. Attitude angle change of the aircraft.

Fig. 13 shows the landing process of a seaplane. The initial attitude angle of the plane is 5°, the initial horizontal speed is 45m/s, and the initial vertical speed is 1.5m/s. At 0.5s, the tail of the seaplane drew a deep trench on the water surface, and at 1s, the water wave generated by the impact had obviously spread outward. The actual vertical displacement experienced by the seaplane during landing generally ranges from 1 to 2 meters. The maximum vertical displacement is 1.85 meters and the minimum displacement is 0.8 meters, which accords with the actual situation.
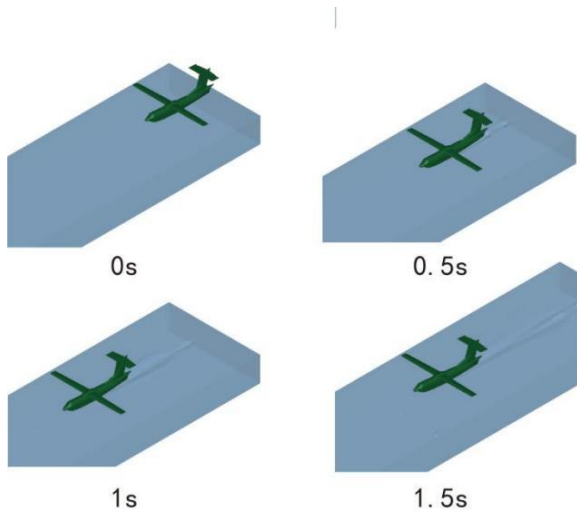
Fig. 13. Landing process of a seaplane.

Fig. 14. Vertical impact force variation curve.

Fig. 15. Pressure curve of P1.

The air cushion is defined as a hermetically sealed layer of air positioned between the free surface and the underlying structure. During the horizontal propagation of waves, the leading edge of the horizontal plate makes contact with the free surface, while the trailing end remains partially submerged or in contact with the flat plate, resulting in air displacement. This process induces deformation in the water's free surface, which subsequently undergoes reformation parallel to the horizontal plate. Even in tranquil water environments, the forward section of the seaplane's underside remains in contact with the water surface. When this part is not completely detached from the water body, the rear section of the aircraft's underside contacts the water surface, creating a substantial enclosed cavity and forming an air cushion.

Fig. 14 presents the vertical impact force curve for an initial attitude angle of 5°. At an initial horizontal velocity of 35 m/s, the maximum impact force is 1251kN. With an initial horizontal velocity of 45 m/s, the maximum impact force reaches 1289kN. Similarly, at an initial horizontal velocity of 63.9 m/s, the maximum impact force is 1275kN. Comparing the three curves in Fig.14, it can be observed that, when the initial vertical speed is same, the maximum impact force remains similar and is largely unaffected by the horizontal speed. However, it is evident from the figure that, with higher initial horizontal velocities, the vertical impact force of the aircraft exhibits relatively small fluctuations after the initial strong impact with the water surface.

Fig. 15 shows the pressure curve at monitoring point P1 with an initial attitude angle of 5°. At an initial horizontal velocity of 35 m/s, the peak pressure at P1 is 23.68kPa. When the initial horizontal velocity is 45 m/s, the peak pressure at P1 reaches 110.3kPa. Interestingly, at an initial horizontal velocity of 63.9 m/s, the pressure at P1 drops to zero. By comparing the three curves in Fig. 15, it can be inferred that the P1 position is located close to the nose of the aircraft, and as the initial horizontal velocity increases, it becomes more challenging for the P1 position to make contact with the water surface within the time interval of 0-2.75s.
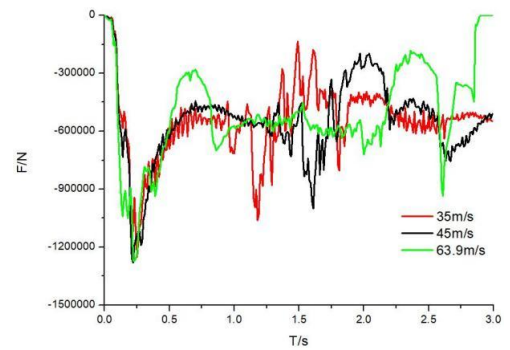
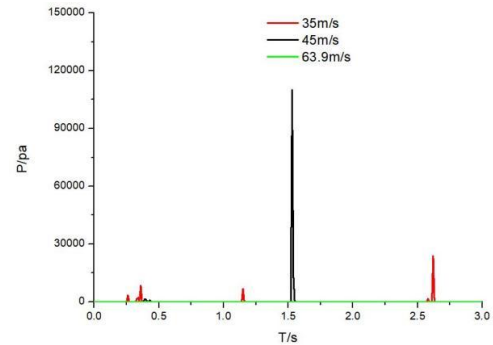Fig. 16 presents the pressure curve at monitoring point P2 with an initial attitude angle of 5°. At an initial horizontal velocity of 35 m/s, the peak pressure recorded at P2 is 2618kPa. With an initial horizontal velocity of 45 m/s, the peak pressure at P2 reaches 2992kPa. Moreover, at an initial horizontal velocity of 63.9 m/s, the P2 monitoring point exhibits a peak pressure of 3489kPa. It is evident that higher initial horizontal velocities lead to greater peak pressures at P2.

Fig. 17 shows the pressure curve at monitoring point P3 with an initial attitude angle of 5°. At an initial horizontal velocity of 35 m/s, the peak pressure observed at P3 is 4124kPa. When the initial horizontal velocity is 45 m/s, the peak pressure at P3 decreases to 3535kPa. However, with an initial horizontal velocity of 63.9 m/s, the P3 monitoring point exhibits a significantly higher peak pressure of 6767kPa. Comparing the three curves in Fig.17, it becomes apparent that lower initial horizontal velocities result in higher pressure values generated by the second impact with the water surface at P3.
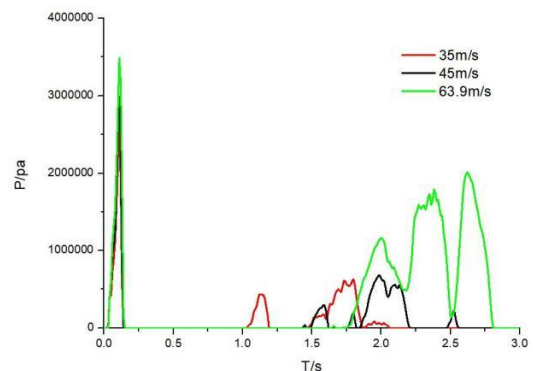
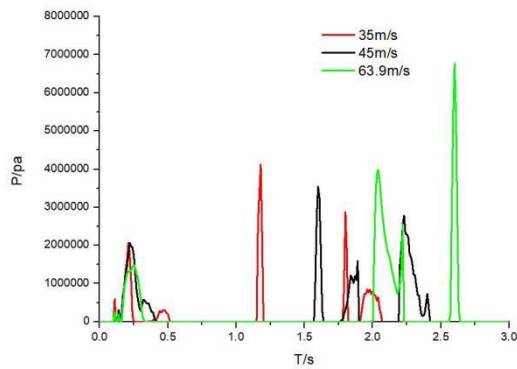

Fig. 16. Pressure curves of P2.

Fig. 17. Pressure curves of P3.

The pressure curves of monitoring points P1, P2, and P3 reveal important insights into the seaplane landing process. During landing, the seaplane initially makes contact with the water surface at monitoring point P2, resulting in a higher pressure value compared to monitoring points P1 and P3. For instance, at an initial horizontal velocity of 35 m/s, contact with the water surface occurs at P2 at 0.11s, leading to a significant pressure surge. At 0.2s, P3 makes contact with the water surface. Affected by the decrease of the impact surface velocity at P2, P3 produces a small pressure value. After 0.25s, P1 experiences a small pressure value influenced by the air cushion formed upon contact with the water surface. At 1.18s, when P3 undergoes secondary contact with the water surface, the pressure increases, surpassing the initial pressure, and an air cushion begins to form, as shown in Fig.18. Subsequently, due to the influence of the air cushion, the elevation angle increase rate decreases, and the elevation angle increases to the maximum value at 1.83 s. At 1.83s, the pressure values at P2 and P3 dropped due to the cushioning of the air cushion, and the tail comes out of the water at 2.6 seconds.

At an initial horizontal velocity of 45 m/s, the interaction between point P2 and the water surface transpires at 0.11s, leading to a notable surge in pressure. Subsequently, at 0.23s, point P3 makes contact with the water surface. Due to the diminished impact surface velocity at P2, P3 registers a diminished pressure value. Following 1.5s, P1 experiences a modest pressure level influenced by the air cushion. By 1.6s, when P3 undergoes secondary contact with the water surface, the pressure exceeds the initial value, resulting in the formation of an air cushion, as shown in Fig. 19. Consequently, influenced by the air cushion, the rate of elevation angle increase diminishes, and the pressure at P3 decreases after 1.6s.

In scenarios with an initial speed of 63.9 m/s, P2 contacts the water surface at 0.1s, generating a substantial pressure. At 0.24s, P3 also makes contact with the water surface, producing a reduced pressure value due to the decreased impact surface

velocity at P2. At 2.0s, during P3's secondary contact with the water surface, the pressure surpasses the initial moment's value, and no air cushion is formed when connected with the air, as shown in Fig. 20. Subsequently, the pressure values at monitoring points P2 and P3 remain relatively high, displaying no significant drop or buffering effect. Throughout this period, P1 remains unaffected with a pressure value of zero. The horizontal speed exhibits minimal influence on the vertical impact force. For this specific seaplane structure, lower speeds result in higher pressure values generated by the tail during secondary impact on the water surface, whereas higher initial horizontal velocities yield greater pressure values during the initial contact with the water surface.
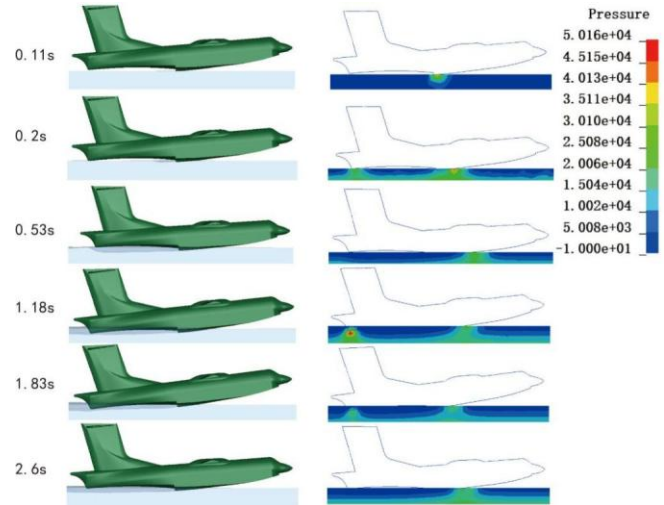

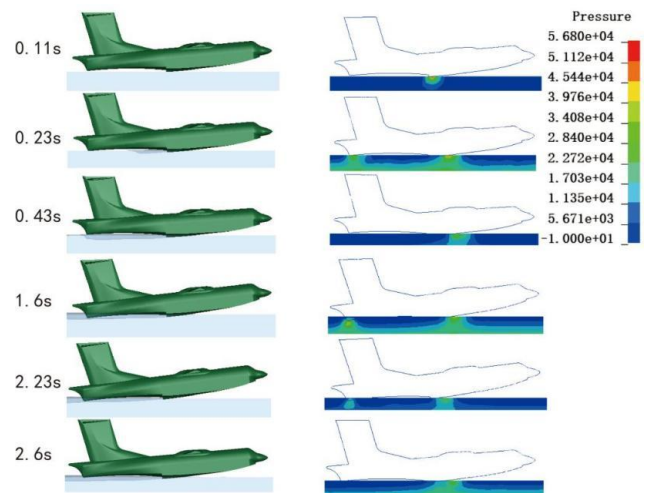Fig. 18. Field and pressure distribution under 35m/s.

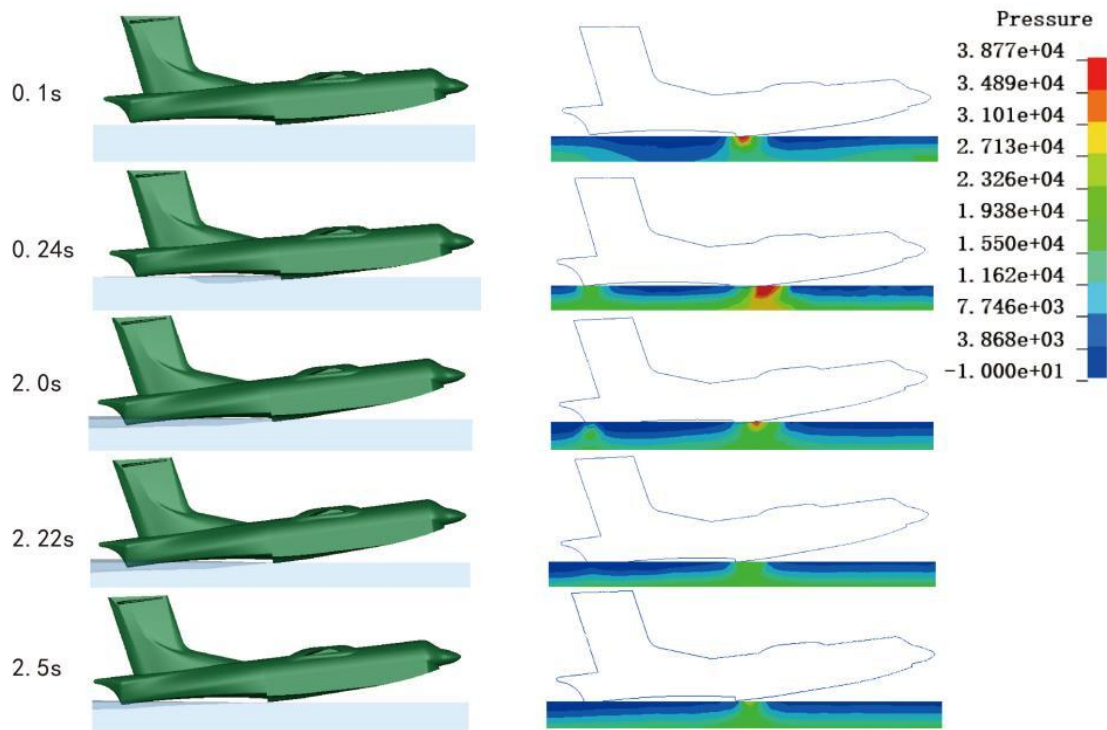Fig. 19. Field and pressure distribution under 45m/s.

Fig. 20. Field and pressure distribution under 63.9m/s.

B. Attitude Angles Analysis

This paper presents a systematic investigation of the seaplane landing process, with a focus on analyzing the changes in attitude angle and acceleration. The study explores the behavior of the air cushion formed during the landing process and examines the variations in impact forces at different stages, as well as pressure at various positions.

Fig. 21 illustrates the vertical acceleration changes of the seaplane at an initial speed of 45m/s. For an initial attitude angle of 5°, the maximum vertical acceleration is measured at 13.2m/s². With an initial attitude angle of 8°, the maximum vertical acceleration reaches 18.7m/s². Moreover, an initial attitude angle of 10° results in a maximum vertical acceleration of 29.7m/s². By comparing the three curves in Fig. 21, it is evident that the vertical acceleration increases as the initial attitude angle becomes larger. Following the initial impact, a smaller attitude angle leads to a narrower range of vertical acceleration for the seaplane, exhibiting a similar trend.

Fig. 22 depicts the changes in attitude angle for an initial level speed of 45m/s, highlighting variations under different attitude angles. The seaplane initially experiences a decrease in attitude angle, followed by an increase, and subsequently a decrease. During the impact, the seaplane tilted forward at a certain angle and then its attitude angle increased. At an initial attitude angle of 5°, the minimum and maximum attitude angles are measured at 3.07° and 7.64°, respectively. For an initial attitude angle of 8°, the minimum and maximum attitude angles are 1.59° and 8.65°, respectively. Similarly, an initial attitude angle of 10° results in a minimum attitude angle of 1.93° and a maximum attitude angle of 8.38°. Notably, no significant rollover occurs within the first three seconds for all three working conditions.
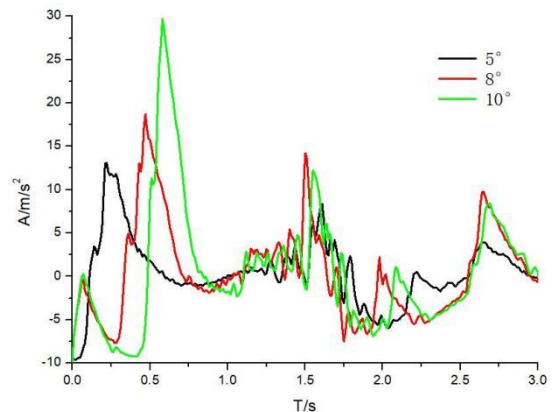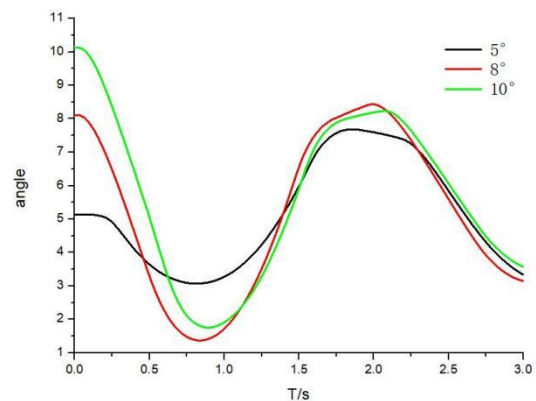

Fig. 21. Vertical acceleration comparison.

Fig. 22. Posture angle comparison

Fig. 23 shows the pressure curve of the seaplane with the initial horizontal velocity 45m/s. when the initial attitude angle is 5°, the maximum impact force is 1280kN. When the initial attitude angle is 8°, the maximum impact force is 1560kN. When the initial attitude angle is 10°, the maximum impact force is 2296kN. The larger the initial attitude angle, the greater the vertical impact force.

Fig. 24 shows the pressure curve at monitoring point P1 with an initial horizontal velocity 45m/s. At an initial attitude angle of 5°, the peak pressure recorded at P1 is 110.3kPa. With an initial attitude angle of 8°, the peak pressure at P1 reaches 70.27kPa. Furthermore, at an initial attitude angle of 10°, the peak pressure at P1 is measured at 360.2kPa. It is worth noting that a smaller initial attitude angle corresponds to a lower pressure value generated at the P1 position before 1 second. The proximity of the P1 monitoring point to the nose of the seaplane, combined with the front-heavy weight distribution, influences the pressure generated at the contact between P1 and the water surface.
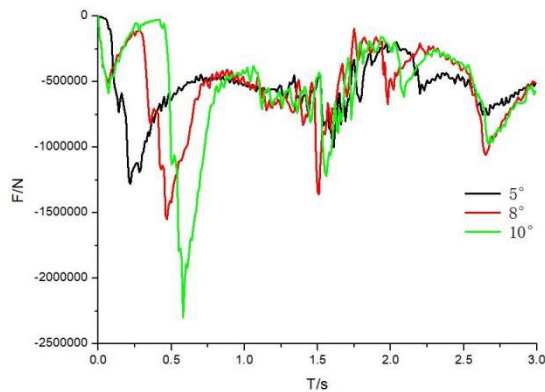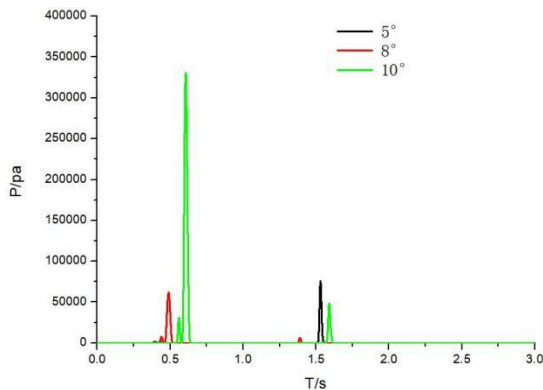

Fig. 23. Comparison of impact force.

Fig. 24. Pressure comparison of P1.

Fig. 25 illustrates the pressure change curve observed at monitoring point P2 with the initial horizontal velocity 45m/s. For an initial attitude angle of 5°, the peak pressure recorded at P2 is 2992kPa. With an initial attitude angle of 8°, the peak pressure reaches 3121kPa. Similarly, at an initial attitude angle of 10°, the peak pressure at P2 reaches 3544kPa. It is observed that a larger initial attitude angle leads to a higher pressure at P2, with a longer time taken to reach the peak pressure. Fig. 26 shows the pressure curve observed at monitoring point P3 with

an initial horizontal velocity of 45m/s. At an initial attitude angle of 5°, the peak pressure recorded at P3 is 3535kPa. With an initial attitude angle of 8°, the peak pressure at P3 reaches 3631kPa. Furthermore, at an initial attitude angle of 10°, the peak pressure is 4406kPa. It is evident that an increase in attitude angle results in a higher pressure generated during the secondary impact of the P3 contact with the water surface.
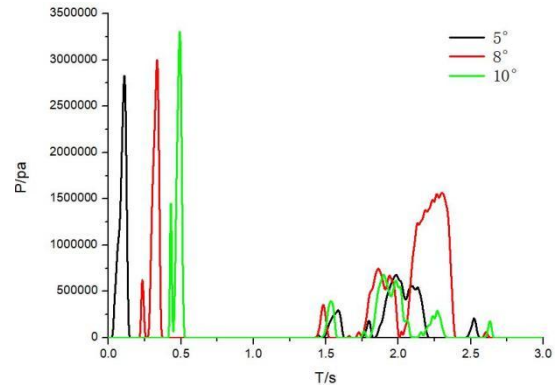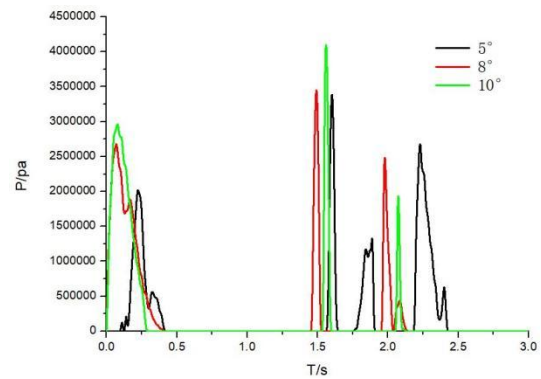

Fig. 25. Pressure comparison of P2.

Fig. 26. Pressure comparison of P3.

The examination of pressure curves at monitoring points P1, P2, and P3 reveals that a greater initial attitude angle results in the seaplane's contact position with the water surface being closer to P3. Specifically, with an initial attitude angle of 5°, contact with the water surface occurs at P2 at 0.11s, resulting in a notable pressure surge. Subsequently, at 0.2s, P3 makes contact with the water surface, producing a reduced pressure value due to the decreased impact surface velocity at P2. Post 0.25s, P1 experiences a modest pressure level influenced by the air cushion formed upon contact with the water surface. By 1.18s, during P3's secondary contact with the water surface, the pressure value exceeds the initial moment's pressure, initiating the formation of an air cushion (see Fig. 18). Consequently, the rate of elevation angle increase diminishes due to the influence of the air cushion, reaching its maximum at 1.83s. At this point, the pressure values at P2 and P3 decrease at 1.83s due to the buffering effect of the air cushion, and the tail emerges from the water surface at 2.6s.

For an initial attitude angle of 8°, P2 contacts the water surface at 0.49s, followed by P3's secondary contact at 1.49s, resulting in an elevated pressure value and the formation of an air cushion (Fig. 27). Influenced by the cushioning air cushion,

the attitude angle increase rate diminishes. At 1.98s, the attitude angle starts decreasing, the air cushion connects with the air, leading to its disappearance, and the pressure values at P2 and P3 are high. The tail disengages from the water surface at 2.6s. With an initial attitude angle of 10°, P2 contacts the water surface at 0.51s, and P1 registers a significant pressure due to its instantaneous air cushion. At 1.56s, the pressure rises as P3 undergoes secondary contact with the water surface, initiating the formation of an air cushion (Fig. 28). At 2.07s, the tilt angle begins decreasing, the air cushion connects with the air, resulting in its disappearance, the pressure value at P3 decreases, and the monitoring point P2, positioned at the contact edge, experiences a floating pressure value. The tail disengages from the water surface at 2.6s.
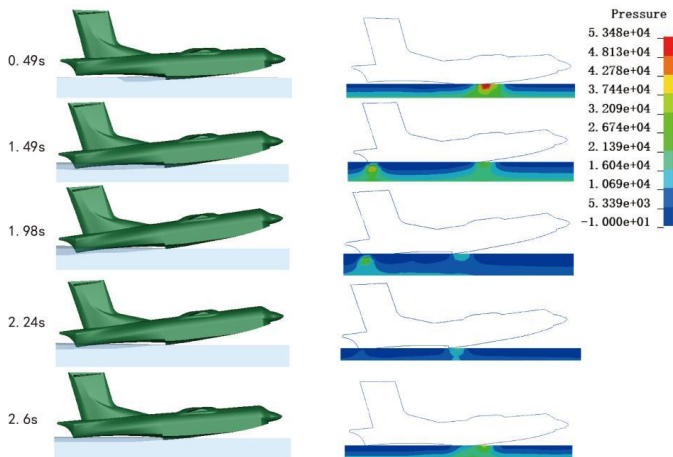

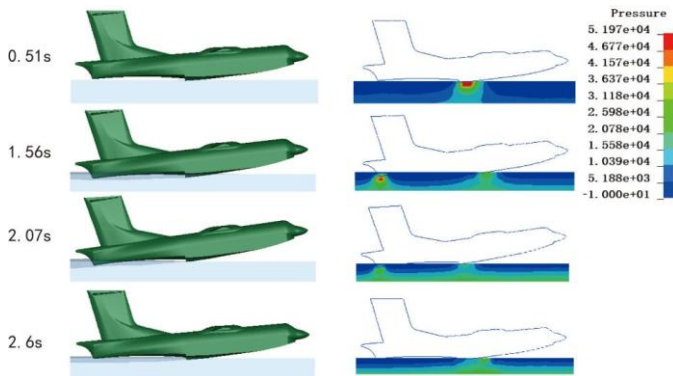Fig. 27. Flow field and pressure distribution with attitude angle 8°.

Fig. 28. Flow field and pressure distribution with attitude angle 10°.

VI. Conclusion

This paper presents a numerical model for studying air-cushion-coupled impact during seaplane landing in a hydrostatic environment. The accuracy of the model was verified by comparison with the cylinder water entry and flat plate impact experiments. Subsequently, the characteristics of air-cushion-coupled impact are investigated under various conditions, including different attitude angles, landing speeds, and impact loads. The conclusions are as follows:

- During the seaplane landing process, the attitude angle shows an obvious peak value within 0 to 3 seconds. Under different initial attitude angles, the maximum

vertical acceleration of the seaplane increases as the initial attitude angle increases. Furthermore, the higher the initial attitude angle, the greater its change rate. The second impact of the aircraft produced greater pressure than the first impact.

- A reduced initial horizontal velocity of the seaplane leads to a diminished increase rate of pitch angle, accentuated cushioning effects of the air cushion, and a lower peak pressure at the monitoring point. When the initial attitude angle is large, the cushioning effect is more obvious, which reduces the peak pressure of the monitoring point.

- To mitigate seaplane structure damage and optimize air cushion utilization, maintaining an optimal landing speed between 30 m/s and 40 m/s is recommended. Furthermore, to prevent rollover and mitigate adverse air cushion effects, the suggested range for the attitude angle is 6° to 8°.

References

[1] Morabito M G. A Review of Hydrodynamic Design Methods for Seaplanes [J]. Journal of Ship Production and Design, 2021, 37;159-180, https://doi.org/10.5957/JSPD.11180039.

[2] Zhang X, Huang J, Huang Y, Huang K, Yang L, Han Y, Wang L, Liu H, Luo J, Li J. Intelligent Amphibious Ground-Aerial Vehicles: State of the Art Technology for Future Transportation[J]. IEEE Transactions on Intelligent Vehicles, 2023, 8(1); 970-987., https://doi.org/10.1109/TIV.2022.3193418.

[3] Washio S. Recent Developments in Cavitation Mechanisms: A Guide for Scientists and Engineers[J]. Recent Developments in Cavitation Mechanisms, 2014.

[4] Tan R, Samuel R T, Cao Y. Nonlinear Dynamic Process Monitoring: The Case Study of a Multiphase Flow Facility[J]. Computer Aided Chemical Engineering, 2017, 40: 1495-1500, https://doi.org/10.1016/B978-0-444-63965-3.50251-8.

[5] Iwanowski B, Fujikubo M,Yao T. Analysis of Horizontal Water Impact of a Rigid Body with the Air Cushion Effect[J]. Journal of the Society of Naval Architects of Japan,1993, 1993(173), 293-302, https://doi.org/10.2534/jjasnaoe1968.1993.293.

[6] Mori Y, Sakai M.Development of a robust Eulerian–Lagrangian model for the simulation of an industrial solid–fluid system[J]. Chemical Engineering Journal,2021, 406: 126841, https://doi.org/10.1016/j.cej.2020.126841.

[7] Hessenthaler A, Balmus M, Röhrle O, Nordsletten D. A class of analytic solutions for verification and convergence analysis of linear and nonlinear fluid-structure interaction algorithms[J]. Computer Methods in Applied Mechanics and Engineering, 2020, 362: 112841, https://doi.org/10.1016/j.cma.2020.112841.

[8] Han K, Feng Y T, Owen D R. Numerical simulations of irregular particle transport in turbulent flows using coupled LBM-DEM[J]. Computer Modeling in Engineering & Sciences, 2007, 18(2), 87-100, https://doi.org/10.3970/cmes.2007.018.087.

[9] Oger G, Doring M, Alessandrini B, Ferrant P.Two-dimensional SPH simulations of wedge water entries[J]. Journal of Computational Physics.2006, 213(2): 803-822, https://doi.org/10.1016/j.jcp.2005.09.004.

[10] Panciroli R, Abrate S, Minak G, Zucchelli A.A. Hydroelasticity in water-entry problems: Comparison between experimental and SPH results[J]. Composite Structures, 2012, 94(2), 532-539, https://doi.org/10.1016/j.compstruct.2011.08.016.

[11] Ahmadzadeh M, Saranjam B, Fard A H, Binesh R A. Numerical simulation of sphere water entry problem using Eulerian–Lagrangian method[J]. Applied Mathematical Modelling, 2014, 38(5-6), 1673-1684, https://doi.org/10.1016/j.apm.2013.09.005.

[12] Facci A L, Porfiri M, Ubertini S.Three-dimensional water entry of a solid body: A computational study[J]. Journal of Fluids & Structures, 2016, 66, 36-53, https://doi.org/10.1016/j.jfluidstructs.2016.07.015.

[13] Serván-Camas B, Cercós-Pita J L, Colom-Cobb J, García-Espinosa J.,Souto-Iglesias A. A. Time domain simulation of coupled sloshing–seakeeping problems by SPH–FEM coupling[J]. Ocean Engineering, 2016,123; 383-396, https://doi.org/10.1016/j.oceaneng.2016.07.003.

[14] Aquelet N, Souli M, Olovsson L. Euler–Lagrange coupling with damping effects: Application to slamming problems[J].Computer Methods in Applied Mechanics & Engineering, 2006,195(1-3); 110-132, https://doi.org/10.1016/j.cma.2005.01.010.

[15] Fourey G, Hermange C, Touzé D L,Oger G.An efficient FSI coupling strategy between Smoothed Particle Hydrodynamics and Finite Element methods[J]. Computer Physics Communications, 2017, 217: 66-81, https://doi.org/10.1016/j.cpc.2017.04.005.

[16] Sun P-N, Le Touzé D, Oger G, Zhang A-M . An accurate FSI-SPH modeling of challenging fluid-structure interaction problems in two and three dimensions[J]. Ocean Engineering, 2021, 221: 108552, https://doi.org/10.1016/j.oceaneng.2020.108552.

[17] Chuang S L. Experiments on slamming of wedge-shaped bodies[J]. Journal of Ship Research, 1967,11(3);190-198, https://doi.org/10.5957/jsr.1967.11.3.190.

[18] Song R, Ren C, Ma X, Qiu L, Lin Z. The study on the anti-impact performance of the oscillating buoy with various air cushions[J]. IET Renewable Power Generation,2021, 15(14): 3459-3471, https://doi.org/10.1049/rpg2.12183.

[19] Ermanyuk E V, Ohkusu M. Impact of a disk on shallow water[J]. Journal of Fluids & Structures, 2005,20(3); 345-357, https://doi.org/10.1016/j.jfluidstructs.2004.10.002.

[20] Chen Z, Xiao X. The simulation analysis of the air cushion in the flat structure enters the water[J]. Journal of Shanghai Jiao Tong University, 2005,39(005);670-673, https://doi.org/10.3321/j.issn:1006-2467

[21] Huera-Huarte F J, Jeon D , Gharib M. Experimental investigation of water slamming loads on panels[J]. Ocean Engineering,2011,38(11-12), 1347-1355, https://doi.org/10.1016/j.oceaneng.2011.06.004.

[22] Zhang J, Wang K, Wan Z Q. Research on prediction method of impact load of two-dimensional wedge into water based on air cushion effect[J]. Ship Science and Technology,2016 ,6(2);1672-7649, https://doi.org/10.3404/j.issn.1672-7649.

[23] Fang X L, Ming F R, Wang P P, Meng F Z, Zhang M A . Application of multiphase Riemann-SPH in analysis of air-cushion effect and slamming load in water entry[J]. Ocean Engineering, 2022, 248: 110789, https://doi.org/10.1016/j.oceaneng.2022.110789.

[24] Adami S, Hu X Y , Adams N A. A new surface-tension formulation for multi-phase SPH using a reproducing divergence approximation[J].Journal of Computational Physics, 2010,229(13);5011-5021, https://doi.org/10.1016/j.jcp.2010.03.022.

[25] Wang L, Xu F,Yang Y. Research on water entry problems of gas-structure-liquid coupling based on SPH method[J]. Ocean Engineering, 2022, 257: 111623, https://doi.org/10.1016/j.oceaneng.2022.111623.

[26] Washino K, Chan E L, Kaji T , Matsuno Y, Tanaka T. On large scale CFD–DEM simulation for gas–liquid–solid three-phase flows[J].

Particuology,2021, 59: 2-15, https://doi.org/10.1016/j.partic.2020.05.006.

[27] Shi Y, Pan G, Yim S C, Yan G, Zhang D. Numerical investigation of hydroelastic water-entry impact dynamics of AUVs[J]. Journal of Fluids and Structures,2019, 91: 102760, https://doi.org/10.1016/j.jfluidstructs.2019.102760.

[28] Liu X, Luo K, Yuan X, Qi B X. Numerical study on the impact load characteristics of a trans-media vehicle during high-speed water entry and flat turning[J].Ocean Engineering,2023, 273: 113986, https://doi.org/10.1016/j.oceaneng.2023.113986.

[29] Peng Y X, Zhang A M,Ming F R. A thick shell model based on reproducing kernel particle method and its application in geometrically nonlinear analysis[J]. Computational Mechanics, 2017,62(3);309-321, https://doi.org/10.1007/s00466-017-1498-9.

[30] Shao J R. Li S M, Liu M B. Numerical Simulation of Violent Impinging Jet Flows with Improved SPH Method[J]. International Journal of Computational Methods, 2016, 13(04): 1641001, https://doi.org/10.1142/S0219876216410012.

[31] Shao J R, Yang Y, Gong H F, Liu B M. Numerical Simulation of Water Entry with Improved SPH Method[J].International Journal of Computational Methods,2019,16(02): 1846004, https://doi.org/10.1142/S0219876218460040.

[32] Yang X, Liu M, Peng S, Huang G C. Numerical modeling of dam-break flow impacting on flexible structures using an improved SPH–EBG method[J]. Coastal Engineering,2016, 108: 56-64, https://doi.org/10.1016/j.coastaleng.2015.11.007.

[33] Khayyer A,Gotoh H, Falahaty H, Shimizu Y.Towards development of enhanced fully-Lagrangian mesh-free computational methods for fluid-structure interaction[J]. Hydrodynamic Research and Progress Series B, 2018, 30: 49-61, https://doi.org/10.1007/s42241-018-0005-x.

[34] Xue B, Wang S-P, Peng Y-X, Zhang M A.A novel coupled Riemann SPH–RKPM model for the simulation of weakly compressible fluid–structure interaction problems[J].Ocean Engineering, 2022, 266: 112447, https://doi.org/10.1016/j.oceaneng.2022.112447.

[35] Sun P, Zhang A M, Marrone S, Ming F. An accurate and efficient SPH modeling of the water entry of circular cylinders[J]. Applied Ocean Research, 2018,72;60-75, https://doi.org/10.1016/j.apor.2018.01.004.

[36] Yang F, Gu X, Zhang Q, Zhang Q.A peridynamics-immersed boundary-lattice Boltzmann method for fluid-structure interaction analysis[J]. Ocean Engineering,2022, 264:112528, https://doi.org/10.1016/j.oceaneng.2022.112528.

[37] Chen X, Rao C Q, Wan D C. Numerical simulation of wedge entry problem by MPS method[J]. Journal of computational mechanics, 2017,34 (3);23-27, https://doi.org/10.7511 / jslx201703013.

[38] Souli M, Ouahsine A,Lewin L. ALE formulation for fluid-structure interaction problems[J]. Computer Methods in Applied Mechanics & Engineering, 2012,190(5-7); 659-675, https://doi.org/10.1016/S0045-7825(99)00432-6.

[39] Hou Z, Sun T, Quan X, Zhang Y G,Sun Z, Zong Z.Large eddy simulation and experimental investigation on the cavity dynamics and vortex evolution for oblique water entry of a cylinder[J]. Applied Ocean Research, 2018,81;76-92, https://doi.org/10.1016/j.apor.2018.10.008.

[40] Ma Z H, Causon D M, Qian L, Mingham G C, Mai T, Greaves D, Raby A. Pure and aerated water entry of a flat plate[J]. Physics of Fluids,2016,28(1);016104, https://doi.org/10.1063/1.4940043.